Check for updates

Programmable icosahedral shell system for virus trapping

Christian Sigl[1], Elena M. Willner[1], Wouter Engelen[1], Jessica A. Kretzmann[1], Ken Sachenbacher[1], Anna Liedl[1], Fenna Kolbe[2,3], Florian Wilsch[2,3], S. Ali Aghvami[4], Ulrike Protzer[2,3], Michael F. Hagan[4], Seth Fraden[4] and Hendrik Dietz[1] ✉

Broad-spectrum antiviral platforms that can decrease or inhibit viral infection would alleviate many threats to global public health. Nonetheless, effective technologies of this kind are still not available. Here, we describe a programmable icosahedral canvas for the self-assembly of icosahedral shells that have viral trapping and antiviral properties. Programmable triangular building blocks constructed from DNA assemble with high yield into various shell objects with user-defined geometries and apertures. We have created shells with molecular masses ranging from 43 to 925 MDa (8 to 180 subunits) and with internal cavity diameters of up to 280 nm. The shell interior can be functionalized with virus-specific moieties in a modular fashion. We demonstrate this virus-trapping concept by engulfing hepatitis B virus core particles and adeno-associated viruses. We demonstrate the inhibition of hepatitis B virus core interactions with surfaces in vitro and the neutralization of infectious adeno-associated viruses exposed to human cells.

For the majority of viral diseases, no effective treatment is available. Broadly applicable antiviral platform technologies do not exist. Here, we propose a platform technology that considers trapping entire virus particles within de novo designed macromolecular shells to inhibit molecular interactions between viruses and host cells (Fig. 1a). We envision shells that can augment and work synergistically with a large variety of virus-binding moieties, whether by themselves neutralizing or not, to create an effective antiviral agent.

To accomplish this function, the shells must on the one hand be large enough to accommodate entire viruses, while also be chemically addressable to allow the inclusion of virus-specificity conferring moieties on the shell's interior surface. The extended surface of the shells enables functionalization in a multivalent fashion. Multivalency can support tight binding of a target virus even for individually weakly virus-binding molecules, as exemplified in previous experiments with phage nanoparticles engineered to trivalently bind influenza A hemagglutinin[1], and with star-shaped DNA aptamer clusters that simultaneously target multiple dengue virus envelope proteins[2]. With shells that fully cover viruses, an even larger degree of multivalency, and thus stronger binding, can be envisioned. Modular functionalization of the shells with virus binders will enable use of the same type of shell platform to target a variety of viruses. Candidate virus binders could be, for example, antibodies, designed proteins[3], nucleic acid aptamers or other polymers[4]. In our concept, the shell material, rather than the moieties directly contacting the virus, will mainly prevent access to the viral surface. Therefore, in principle, any virus-binding molecule could potentially be used to convert the shells into an effective virus-neutralizing trap.

Our shell concept requires the construction of massive molecular complexes that are adaptable to cover the dimensions of viral pathogens (~20–500 nm; ref. [5]), which poses a fundamental nanoengineering challenge. Protein designers have previously succeeded in creating artificial macromolecular cages[6–9]. However, the designed protein cages are much smaller than the vast majority of natural viruses. DNA nanotechnology[10–15] can create discrete objects with structurally well-defined three-dimensional (3D) shapes[16,17], including higher-order objects[18–22] with molecular masses exceeding 1 GDa (ref. [23]). However, these previous designs and the underlying concepts yield objects that are either too small, assemble with insufficient yields, do not match the shapes of viruses or are too flexible or skeletal to be suitable for effectively trapping and occluding entire virus particles.

To build the envisioned virus trap, we created a programmable icosahedral shell 'canvas' by adapting the symmetry principles found in natural viral capsids[24]. Caspar and Klug elucidated the geometric principles that govern the structure of natural viral capsids in 1962 (ref. [25]). According to Caspar and Klug's theory, which has been expanded recently[26], the number of distinct environments occupied by proteins within an icosahedral capsid is described by its triangulation number (T number), which can be computed on the basis of the arrangement of pentamers and hexamers within an icosahedral capsid ($T = h^2 + hk + k^2$, with h and k denoting integer coordinates of pentamers in the hexagonal lattice, Fig. 1b). The total number of proteins required to build a natural capsid is $T \times 60$. This is because natural protein subunits are, by default, asymmetric and homotrimerization is minimally required to construct a three-fold symmetric subunit that can assemble into an icosahedral shell with 20 triangular faces. To build larger capsids, viruses use more than one capsid protein or capsid proteins that can adopt different conformations. The structure of natural virus capsids forms the basis for our synthetic programmable icosahedral shell canvases, which we analogously classify using T numbers.

Shell canvas design principles

To implement the icosahedral canvas concept, we designed pseudosymmetric triangular subunits (Fig. 1c) based on multilayer

[1]Department of Physics, Technical University of Munich, Munich, Germany. [2]Institute of Virology, School of Medicine, Technical University of Munich and Helmholtz Zentrum München, Munich, Germany. [3]German Center for Infection Research, Munich, Germany. [4]Department of Physics, Brandeis University, Waltham, MA, USA. ✉e-mail: dietz@tum.de
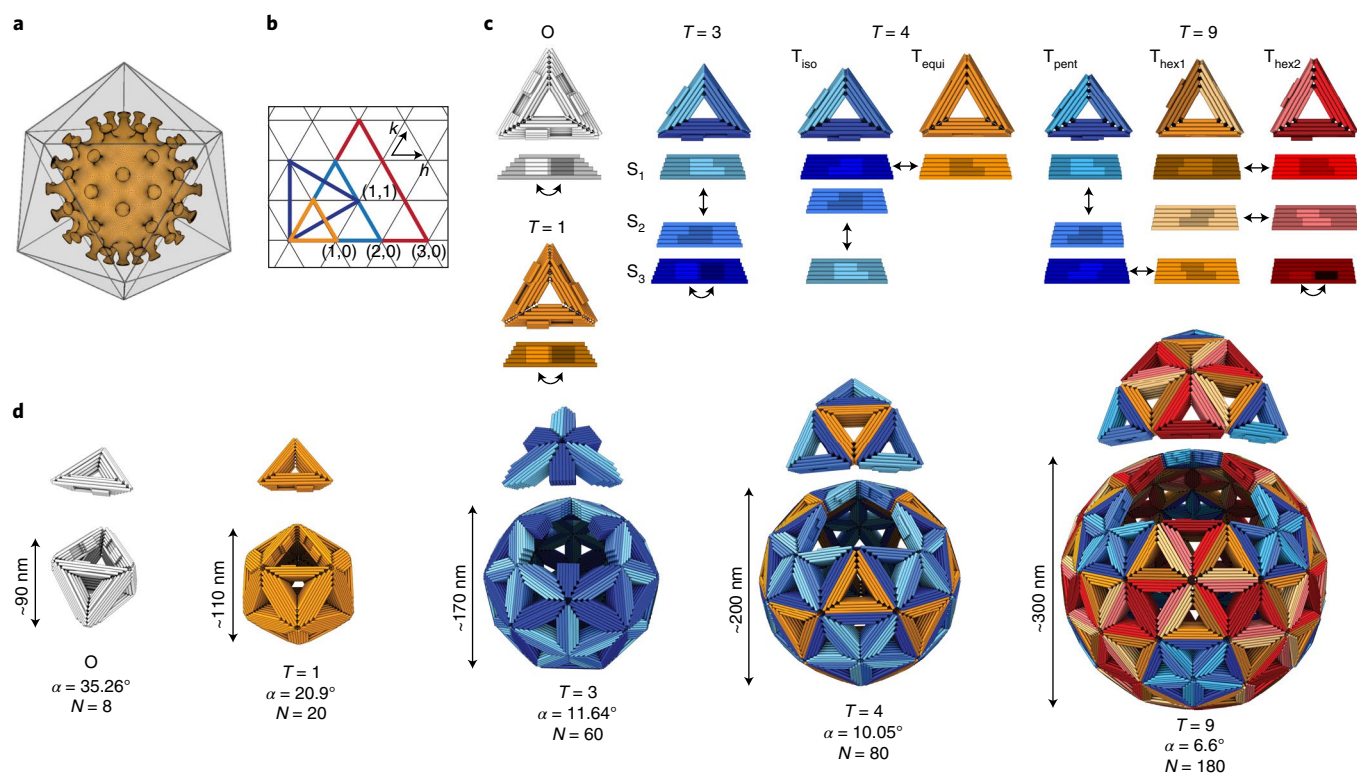
Fig. 1 | Design principles for antiviral platform technologies. a, Icosahedral shell encapsulating a virus capsid. **b**, Triangular net representation of icosahedral shells. Each coloured triangle represents one of the 20 faces forming an icosahedron. The small triangles represent the triangular building blocks. (h,k) indicates the location of pentamers within a shell. **c**, Cylindrical models of DNA origami triangles assembling into the shells shown in **d**. The edges of the triangles are bevelled and modified with shape-complementary protrusions (light) and recesses (dark). The arrows indicate shape-complementary combinations. Subscripts (such as 'pent') on T refer to triangle names; S_1 to S_3 number the sides of each triangle. For design details, see Supplementary Figs. 37–40. **d**, The octahedral and icosahedral shells formed by the triangles shown in **c**. For each shell design, one of the polyhedral faces has been displaced (see **b**) to help show the polyhedral symmetry. O, octahedral; T, T number; α, the bevel angle of the sides of the triangles; N, the number of DNA origami triangles building the shell.

DNA origami concepts[11,12]. Each side of a triangular subunit is the equivalent of one protein subunit of a natural viral capsid. The overall canvas scale and type are controlled by geometric instructions provided by the triangular subunits. These instructions are given by the choice of length, the topological binding pattern[27] and the bevel angle of each triangular edge. Because in our system each triangular edge represents one protein, Caspar and Klug's T number gives the number of unique triangular edges required to build a particular icosahedral canvas shell. Hence, $T = 1$ and $T = 3$ shells may both be built with a single triangle, with three identical edges for $T = 1$ and three different edges for a $T = 3$ shell (Fig. 1c,d, left). A $T = 4$ shell requires two separate triangular subunits, for example, one triangle with three unique edges and another with three identical edges (Fig. 1c,d, middle). A $T = 9$ shell requires three different triangles, each having three unique edges (Fig. 1c,d, right). The greater the T number, the greater the overall number of triangles per target shell, given by $20T$. We used design solutions in which all triangle bevel angles for a particular target shell were the same. While $T = 9$ was the largest canvas we set out to build, we also designed triangular subunits for a smaller octahedral container (O, Fig. 1c,d, left).

Subunit and shell canvas assembly

We used iterative design with caDNAno (ref. [28]) paired with elastic network-guided molecular dynamics simulations[29] to produce candidate designs. To approximate the target bevel angles, we tuned the helical connectivity of the triangle edges at the vertices (Supplementary Fig. 1). These candidate designs were encoded

in DNA sequences using the methods of DNA origami[10,11] and self-assembled in one-pot reaction mixtures[30]. Gel-electrophoretic folding quality analysis demanded some design iterations to improve triangular subunit assembly yields (Supplementary Fig. 2). To validate the 3D structures of the designed triangles, we studied all triangle subunits using cryo-electron microscopy (cryo-EM) single particle analysis (Fig. 2). The resulting 3D electron maps had resolutions ranging from 13 to 22 Å (Supplementary Figs. 3–10), which allowed us to evaluate the overall 3D shapes, the observed versus desired bevel angles (Supplementary Table 1, deviations within 5°), the correct formation of the binding patterns and the occurrence of systematic folding defects. For instance, one triangle variant (T_{hex1}) had a defective vertex, which decreased its ability to form lateral edge-to-edge interactions (Supplementary Fig. 11). Based on the cryo-EM data, we refined the design and eliminated the defect.

The triangle variants self-assembled (see Methods) successfully into the designed icosahedral shells, as confirmed by direct imaging by cryo-EM (Fig. 2a and Supplementary Figs. 12–16). Inspection of individual particles (Fig. 2a) and two-dimensional (2D) class averages (Fig. 2b–f) revealed particles displaying the designed symmetries. For example, the three symmetry axes of the octahedron (four-, three- and two-fold, Fig. 2b) and $T = 1$ (five-, three- and two-fold, Fig. 2c) shells can be clearly seen. For the higher-T-number shells, the underlying triangular net predicted from the Caspar and Klug representation became clearly visible (Fig. 2d–g). We determined 3D EM maps from the image data by imposing the respective symmetry (Fig. 2b–e). The resulting
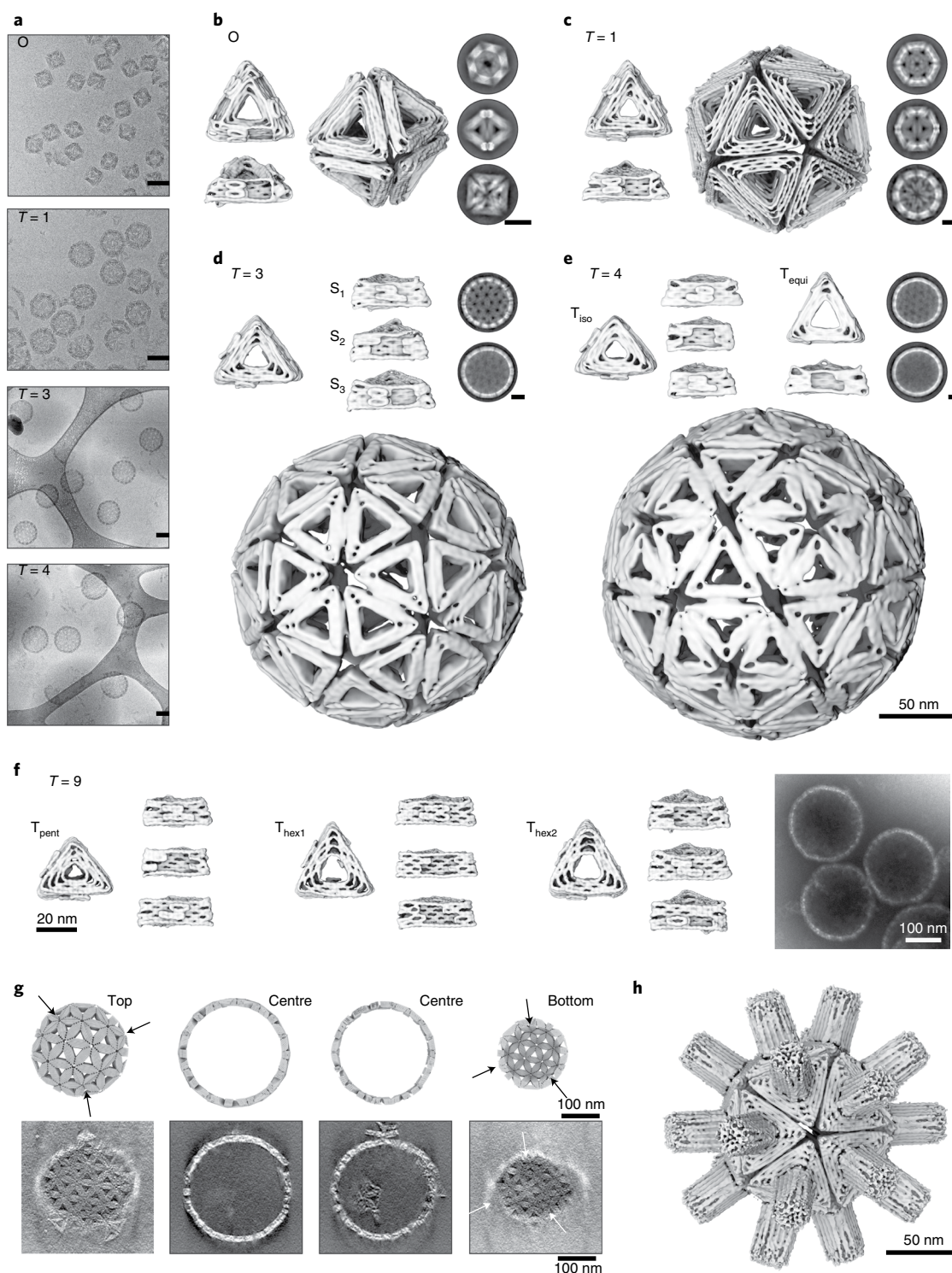
Fig. 2 | Structures of shells and shell subunits. a, Cryo-EM micrographs of assembled shells in free-standing ice (O, $T=1$) and on lacey carbon grids with carbon support ($T=3$, $T=4$). Scale bars, 100 nm. **b**–**e**, Cryo-EM reconstructions of shell subunits and fully assembled shells for O (**b**), $T=1$ (**c**), $T=3$ (**d**) and $T=4$ (**e**) shells. The 2D class averages show assembled shells from different orientations. Scale bars, 50 nm. See also Supplementary Videos 1–4. **f**, Cryo-EM reconstructions of the three triangles assembling into a $T=9$ shell and a negative-stained EM micrograph of the assembled shells. **g**, Comparison of slices through a model $T=9$ shell with the slices of a tomogram calculated from a negative stain EM tilt series. The arrows indicate the positions of pentamers within the $T=9$ shell (Supplementary Video 5). **h**, Cryo-EM reconstruction of a $T=1$ shell with a DNA 'spacer' module blocking the central cavity (Supplementary Video 8).

maps had resolutions ranging from 20 to 40 Å. For the octahedron and $T=1$ shells, the 3D maps reconstructed without imposing any a priori symmetry superimposed well the sibling maps

reconstructed with imposed symmetry (Supplementary Figs. 12 and 13). We classified and treated the cryo-EM maps of shells that lacked one or multiple triangles separately from complete shells to
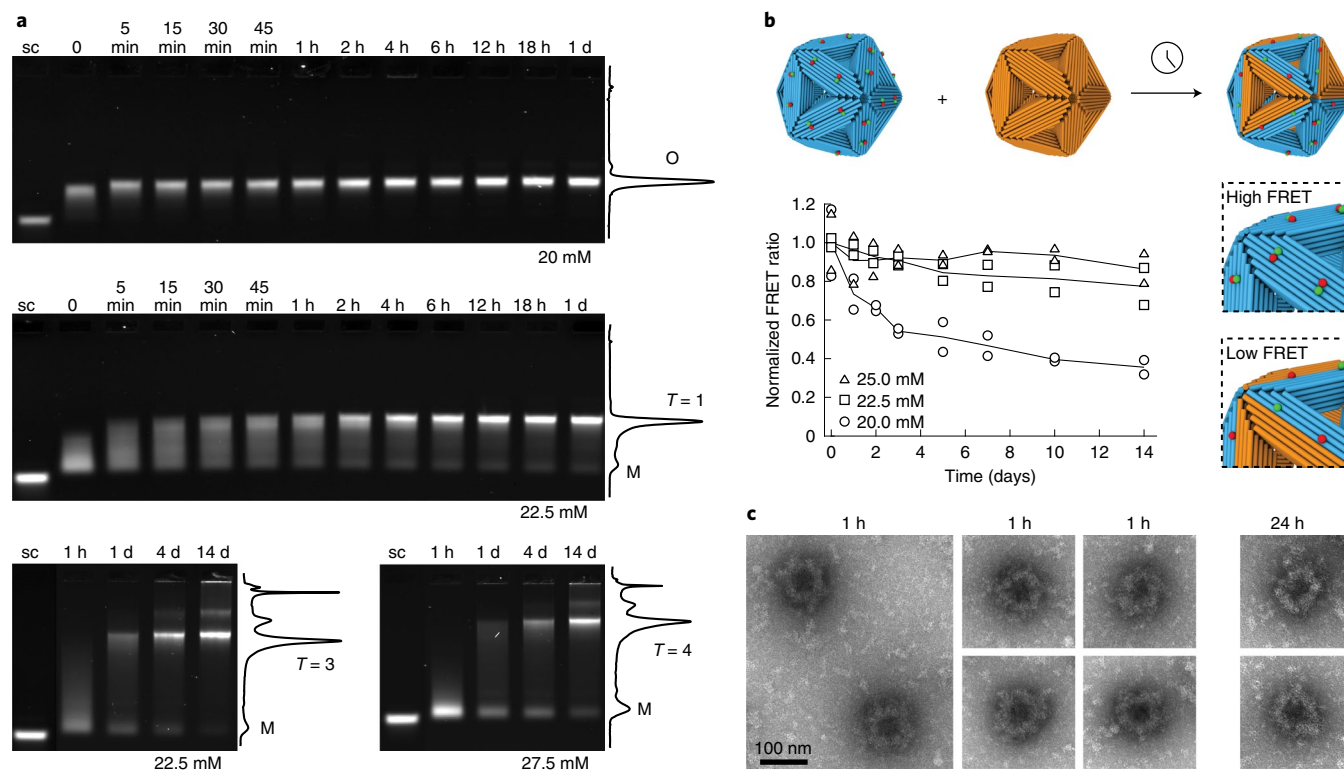
Fig. 3 | Shell yield and stability. a, Laser-scanned fluorescent images of 0.5% agarose gels showing the assembly of octahedra, $T=1$, $T=3$ and $T=4$ shells at 40 °C with a monomer concentration of 5 nM at different time points. The MgCl$_2$ concentrations of the gels are specified at the bottom right. The solid lines show the cross-sectional lane intensity profiles of the 1 day (O, $T=1$) and 14 day samples ($T=3$, $T=4$). M represents the free triangle monomers. sc indicates the M13-8064 scaffold strand as reference. **b**, Triangle exchange experiments. Förster-resonance-energy-transfer (FRET)-pair labelled $T=1$ shells are shown in cyan; unlabelled shells are shown in orange. The graph plots the FRET signals measured at different incubation times in the presence of the indicated concentrations of Mg^{2+} for $n=2$ independent measurements (for design details, see Supplementary Fig. 44). Insets show a high FRET signal if both neighbouring triangles are modified with fluorescent dyes, and a low FRET signal if only one triangle is modified. **c**, Negative staining TEM images of octahedral shells coated with a 1:1 mixture of oligolysine and PEG–oligolysine and incubated for 1 and 24 h in 55% mouse serum at 37 °C. The scale bar in **c** refers to all panels in **c**.

assess quality and yield (Supplementary Figs. 12 and 13). The largest $T=9$ shells were imaged using negative stain EM tomography (Fig. 2f,g and Supplementary Fig. 17). Sections through the tomograms of assembled $T=9$ shells revealed fully closed shells as well as the correct arrangement of pentamers according to the designed T number (arrows in Fig. 2g and Supplementary Fig. 17).

To elucidate the effects of the orientational specificity of subunit−subunit interactions, we varied the bevel angle of the $T=1$ subunits from the ideal geometry ($\alpha = 20.9°$). We designed two additional variants of the $T=1$ triangle in which the bevel angles deviated by $+5°$ or $-5°$ from the icosahedral ideal. The decrease or increase in the bevel angle caused the appearance of larger or smaller, often defective, assemblies in addition to $T=1$ shells, respectively (Supplementary Fig. 18). Based on these data, we conclude that the correct target bevel angle in a $T=1$ triangle subunit must be matched within a range of $\pm5°$.

To demonstrate a route for sealing the remaining cavities in the shells, we built DNA bricks with a triangular cross-section roughly corresponding to the dimensions of the triangular cavities in the shell subunits. We anchored the bricks through multiple attachment points to the outer surface of $T=1$ shell triangles (see Supplementary Fig. 19 for design details and Supplementary Fig. 20 for a cryo-EM map). We solved the structure of the spiky $T=1$ shell using cryo-EM single particle analysis (Fig. 2h and Supplementary Fig. 21). The resulting map overlaps well with those of the unmodified $T=1$ shell, but the central cavities of the triangle subunits are

now blocked by the added brick modules (Supplementary Fig. 21). The fact that the plugging of the cavities with the DNA bricks worked indicates the robustness and structural modularity of our shells. The brick may also be considered as a mimic for the previously described DNA-based membrane channels[31], or for any other functional module that one wishes to attach to a shell.

Shell yield and stability

We evaluated practical aspects such as assembly yield and stability in physiological conditions in which the system is ultimately expected to be applied. Low-density gel-electrophoretic mobility analysis (Fig. 3a and Supplementary Fig. 22) revealed shell assembly proceeded by the disappearance of the triangular monomers, the appearance of a smear indicating the presence of oligomeric species, followed by the emergence of a dominant high-intensity band corresponding to the fully formed shells. The octahedral and $T=1$ shells formed within 15 and 60 min, respectively, which is sufficiently fast to enable the self-assembly of these shells directly during the one-pot triangle-folding reaction (Supplementary Fig. 23). They formed with a final complete shell yield of ~95 and ~70%, respectively. The $T=3$ and $T=4$ shells formed with a yield of about 40% (Fig. 3a). Subunit-exchange experiments with fluorescently labelled subunits revealed that under shell-favouring conditions triangles that are incorporated into closed shells do not exchange with solution (Fig. 3b and Supplementary Fig. 24). Under equilibrium conditions, triangles do exchange (Fig. 3b and Supplementary Fig. 24).
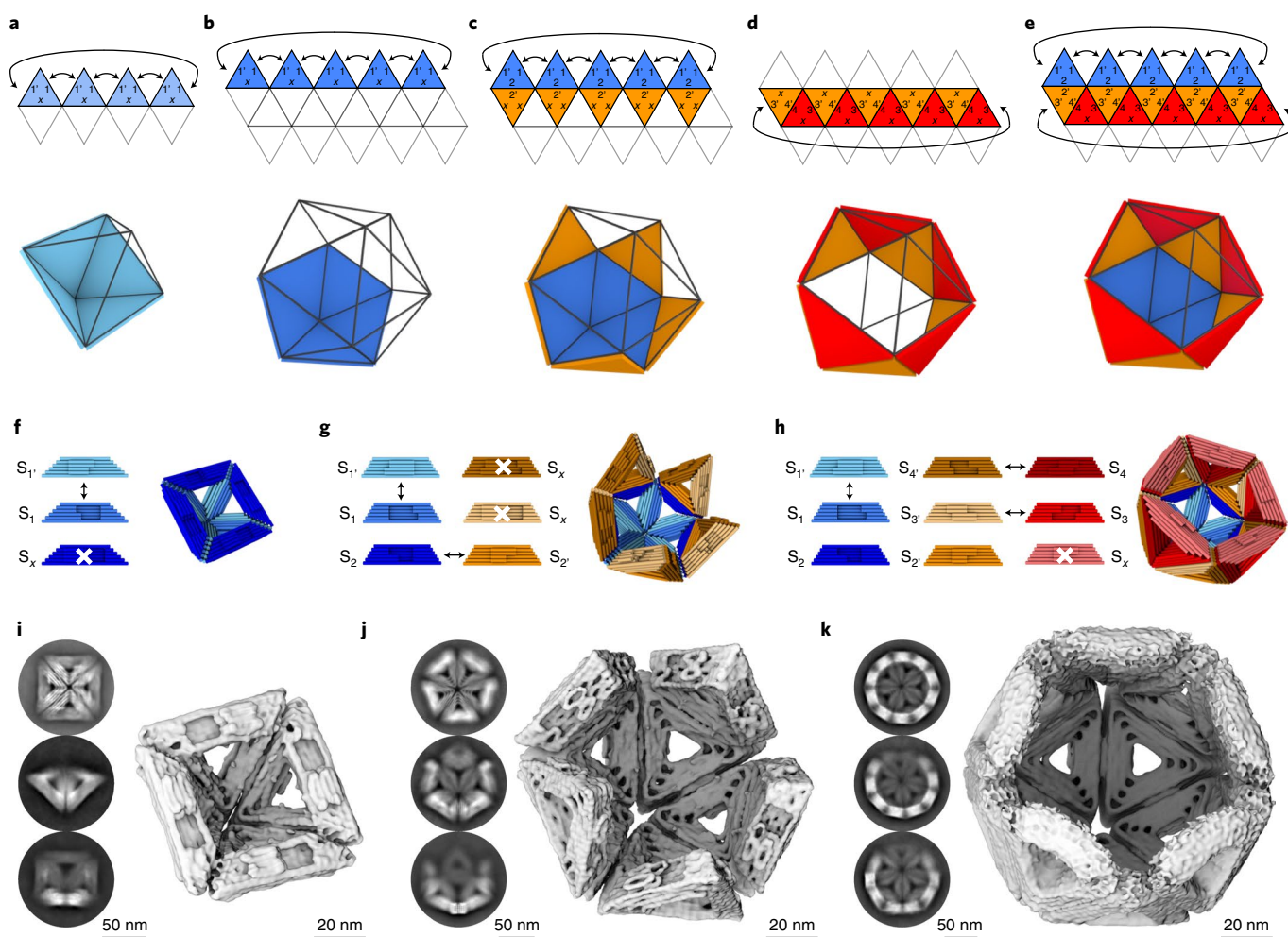
Fig. 4 | Sculpting on an icosahedral canvas. a–e, Triangular net projections and schematics of different partial shells: half octahedral shell (**a**), pentamer (**b**), half $T=1$ shell (**c**), ring (**d**) and $T=1$ shell lacking a pentagon vertex. The numbers indicate complementary edges. x indicates the number of deactivated edges. (**e**). **f–h,** Cylindrical models of the DNA origami triangles and the corresponding partial shells of the half octahedral shell (**f**), the half $T=1$ shell (**g**) and the $T=1$ shell lacking a pentagon vertex (**h**). The sides of the triangles are modified with protrusions and recesses. The arrows indicate shape-complementary sides. White crosses indicate deactivated interaction sites. S_x indicates the edge number shown in **a** to **e**. For design details, see Supplementary Figs. 41 and 42. **i–k,** Cryo-EM 3D reconstructions of the partial shells shown in **f–h** and typical 2D class averages showing the assembled shells from different orientations.

To stabilize the shells for application in physiological fluids, we first assembled the shells and then applied ultraviolet (UV) point welding[32] to create additional internal covalent bonds across the stacking contacts in the triangle subunits. We then coated the shells with a mixture of oligolysine and poly(ethylene glycol) (PEG)–oligolysine[33]. This two-step treatment allowed us to successfully transfer the shells into mouse serum, in which the shells remained intact for up to 24 h (Fig. 3c).

Sculpting on the icosahedral canvas
By changing the geometry of the shape-complementary topographic features, the triangular subunits can be programmed to cover only user-defined areas on the icosahedral canvas. To create full shells, only the minimum number of different topographic interaction patterns ('symmetries') is implemented, as discussed above. Introducing additional types of topographic edge-to-edge interactions per triangular subunit allows a reduction of the symmetry in which the subunit may be integrated into the canvas. Furthermore, the stacking interactions can be modularly activated and deactivated, for example, by shortening a strand terminus involved in a

stacking contact or by adding unpaired thymidine terminal strand extensions. Together, these features enable the sculpting of a variety of objects on the icosahedral canvas in a programmable fashion, including full shells, pentagonal vertices, (spherical) half shells and shells with virus-sized openings, using rational design decisions.

To design such objects, we used the triangular net projection of the chosen icosahedral canvas type as a drawing board (Fig. 4a–e). For example, to prepare half instead of full octahedra, complementary lock-and-key interactions of two edges of the triangular subunit are needed and one edge interaction must be deactivated (Fig. 4a). A pentagonal dome can be analogously created based on the $T=1$ icosahedral canvas (Fig. 4b). Building an icosahedral half shell requires two different triangular subunits, one that forms the pentagonal dome, and another that specifically docks onto the edges of the pentamer (Fig. 4c). A ring-like 'sheath' may also be built by two triangles (Fig. 4d). To build a $T=1$ shell variant with one missing pentagon vertex, three triangular subunit variants with a specific interaction pattern are needed (Fig. 4e). We practically implemented the above discussed design variants using appropriately modified triangular building blocks (Fig. 4f–h and
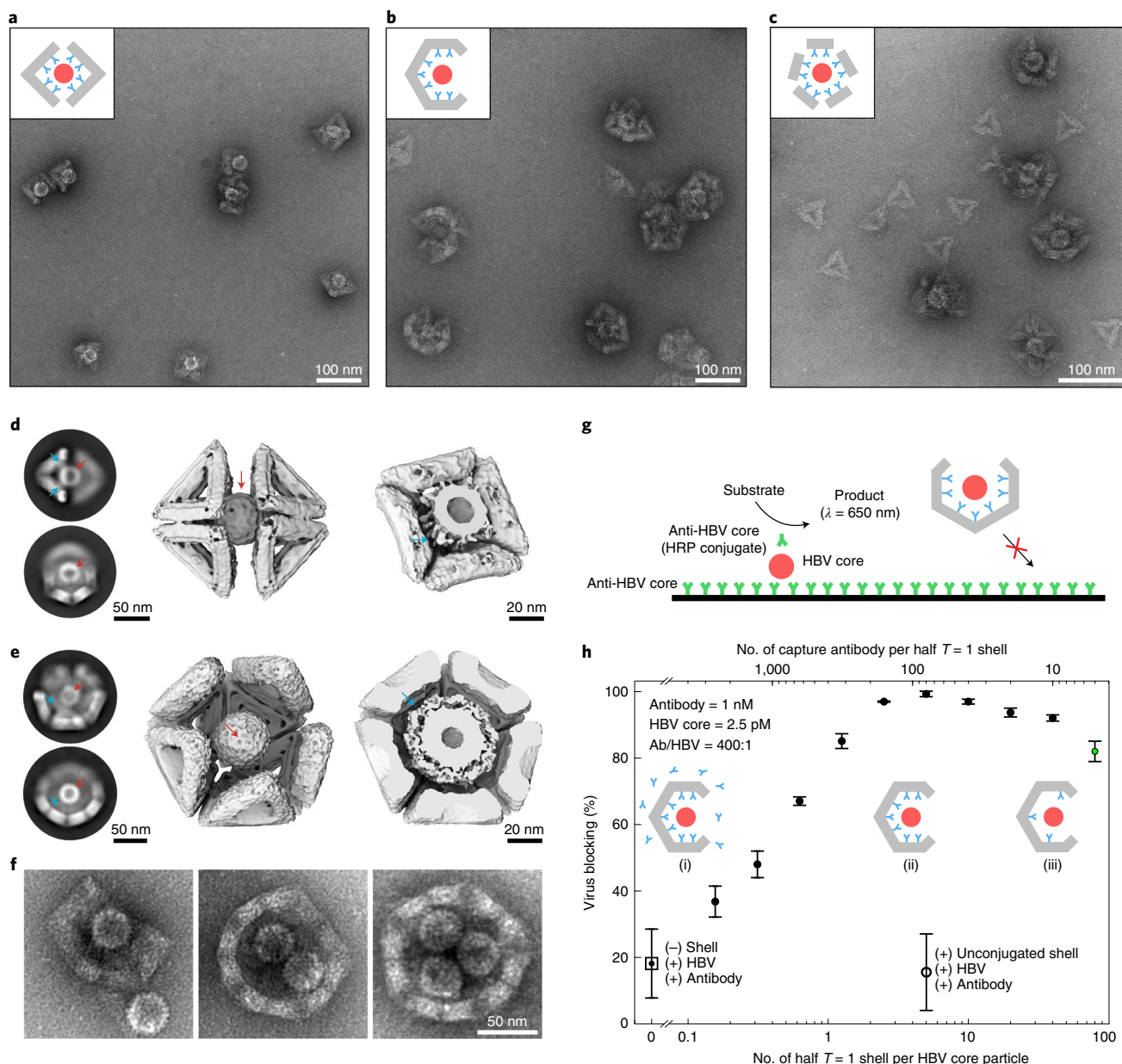
Fig. 5 | Trapping of HBV core particles. a–c, Negative stain TEM images of HBV core particles trapped in octahedral half shells (**a**), half $T=1$ shells (**b**) and monomeric $T=1$ triangles, with each triangle modified with nine antibodies self-assembled around the HBV core particle (**c**). Insets: schematic representations of the shell structure (grey) equipped with antibodies (cyan) with a trapped HBV core particle (red). **d,e,** Two-dimensional cryo-EM class averages (left), cryo-EM reconstruction (middle; Supplementary Videos 6 and 7) and a cut through the cryo-EM map (right) of two octahedral half shells (**d**) and the $T=1$ half shell (**e**) coordinating a trapped HBV particle. Red arrows, HBV core particle; cyan arrows, antibodies connecting the shell to the HBV core particle. In **d**, the density around the HBV core particle stems from the antibodies connecting the HBV core particles to the octahedral shell. The electron density thresholds differ in **d** and **e**, which makes the HBV core particle look thicker in the $T=1$ half shell compared with the half octahedron. The scale bar in **d** refers to all panels in **d**. **f,** Negative stain TEM images of $T=1$ shells with a missing pentagon vertex engulfing up to three HBV core particles. The scale bar in **f** refers to all panels in **f**. **g,** Schematic representation of the in vitro virus-blocking enzyme-linked immunosorbent assay (ELISA) experiment. **h,** In vitro virus-blocking ELISA experiments. All experiments were performed with a ratio of antibody (Ab) to HBV of 400:1. The half shells have 90 antibody binding sites. The filled circles indicate 2.5 pM HBV core particles incubated with pre-assembled mixtures of 1 nM oligonucleotide-conjugated capture antibody and various concentrations of half $T=1$ shells. Insets: low half-shell concentration in which antibodies saturate the half-shell binding sites and excess antibodies are in solution (i), the half shells are saturated with antibodies with few antibodies remaining in solution (ii) and high half-shell concentration in which antibodies do not saturate all half-shell binding sites (iii). Controls: the open circle represents a mixture of HBV core particles, antibodies and unfunctionalized $T=1$ half shells; the open square represents HBV and antibodies without half shells. The green dot shows a blocking efficiency of about 80% for a 5:1 ratio of Ab/half shells. The data are presented as mean ± s.d. (standard deviation) for $n=3$ independent measurements.

Supplementary Fig. 25). The building blocks self-assembled successfully into the desired higher-order objects based on their icosahedral canvas, which we validated experimentally by determining their cryo-EM solution structures (Fig. 4i–k and Supplementary Figs. 26–28) and negative stain transmission electron microscopy (TEM) images (Supplementary Fig. 29).
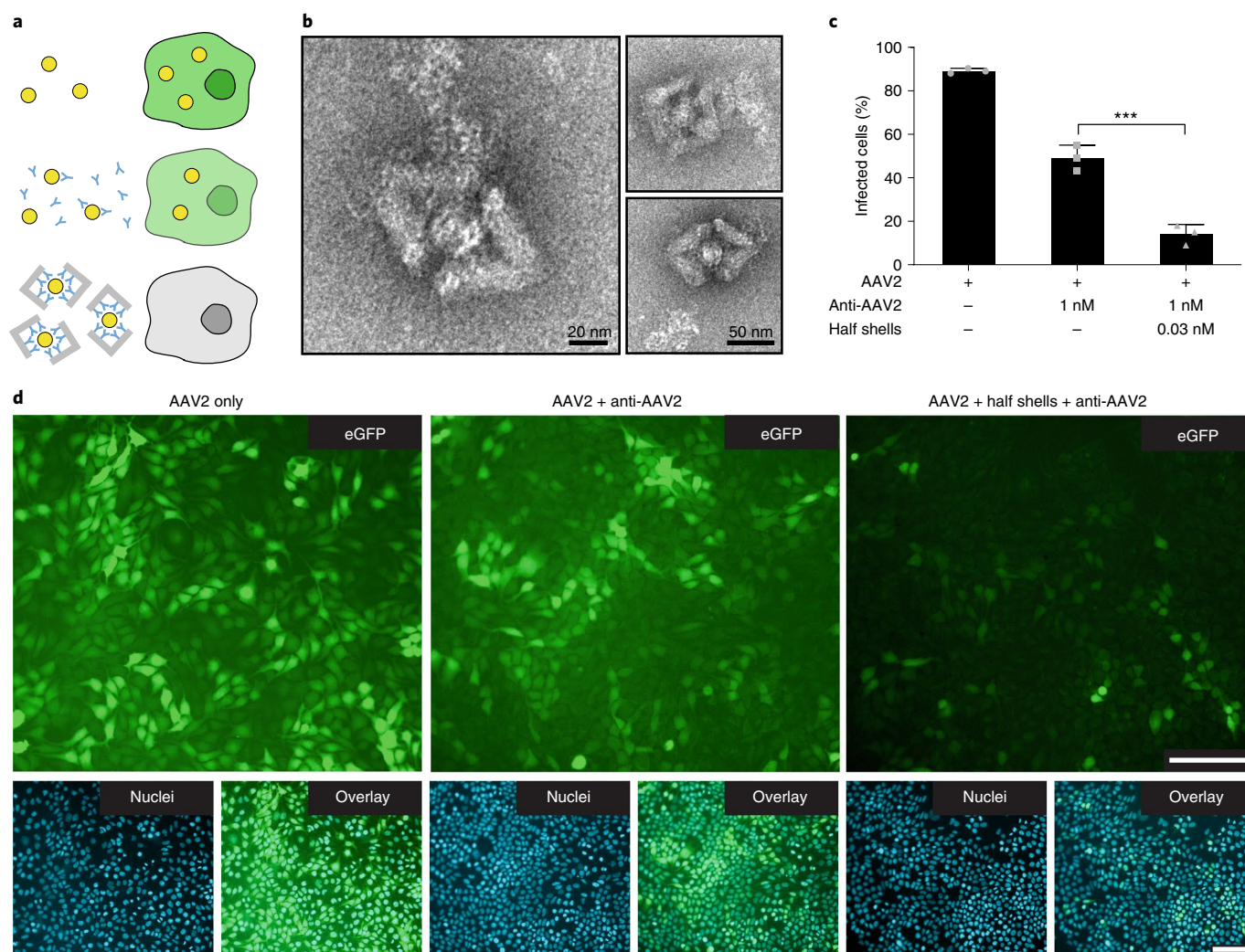
Fig. 6 | Neutralization of AAV2 with DNA origami half shells. a, Schematic illustrating that successful infection of HEK293T cells (human embryonic kidney cell line) with AAV2 results in the expression of eGFP (top), the infection of HEK293T cells with AAV2 is reduced in the presence of free anti-AAV2 (middle), whereas cells exposed to AAV2 captured in DNA half shells do not express eGFP (bottom). Yellow circles, AAV2; blue Y, anti-AAV2 IgG antibodies; grey angled blocks, DNA half shells. **b**, Negative stain TEM images demonstrating the capture of AAV2 virus particles within the DNA origami half shells. Capture was successful in the presence of BSA. **c**, Quantification of infected cells by flow cytometry for conditions with AAV2 only, AAV2 with anti-AAV2 at the IC_{50} concentration (1 nM) and AAV2 with DNA origami half shells with anti-AAV2 conjugated to the inside. Anti-AAV2 and DNA half shells were pre-incubated with AAV2, respectively. The half shells were used at an overall identical antibody concentration as in the anti-AAV2-only condition, with ~36 antibodies per shell and ~7 half shells per virus particle. The data were quantified using flow cytometry and are presented as mean ± s.d. (standard deviation) for $n = 3$ biologically independent experiments. Individual data points are overlayed. One-way analysis of variance (ANOVA) was performed to test statistically significant inhibition compared with the control. Both anti-AAV2 alone and half-shell origami + anti-AAV2 demonstrated statistically significant neutralization compared with the AAV2-only control ($P \le 0.0001$). Conjugation of anti-AAV2 to DNA origami half shells resulted in statistically significantly greater neutralization capacity than free anti-AAV2 ($P = 0.0002$, ***$P \le 0.001$). **d**, Representative epifluorescent microscopy images demonstrating the expression of eGFP by infected cells. The images are representative of one of $n = 3$ biologically independent experiments; similar results were observed each time. For each of the conditions, eGFP expression (green), cell nuclei (blue) and the overlay are given. Scale bars, 100 μm.

Virus trapping

Viruses can be trapped in, or coordinated by, pre-assembled icosahedral shell segments featuring sufficiently large apertures (Fig. 5a,b and Supplementary Fig. 30). Alternatively, protective shells can be formed directly on the surface of virus particles (Fig. 5c). Both approaches are illustrated in experiments we performed with hepatitis B virus (HBV) core particles (Fig. 5a–c, insets, red). To confer specificity to HBV, we conjugated antibody anti-HBc 17H7 (isotype IgG-2b) to the DNA shells through the hybridization of single-stranded DNA (ssDNA)-labelled antibodies to a set of anchor points on the triangle subunits (Fig. 5a–c, insets, cyan). We did not observe any HBV binding in the absence of the HBV

antibodies (Supplementary Fig. 31), nor in the presence of antibodies specific to other targets (Supplementary Fig. 31).

We recorded 3D cryo-EM maps of octahedral and $T = 1$ half shells with trapped HBV core particles (Fig. 5d,e and Supplementary Figs. 32 and 33). For the half-octahedral variant, the majority of particles consisted of two opposing half octahedra coordinating a single HBV core particle in their middle (Fig. 5d and Supplementary Fig. 32). The micrographs and cryo-EM map also reveal signatures reflecting the antibodies that link the DNA shell to the trapped HBV core particle (Fig. 5d, right). Similar antibody signatures may be found in the image data for the half $T = 1$ shell–HBV complex (Fig. 5e, right). We also trapped HBV core particles in larger $T = 1$

shell variants with a missing pentagon vertex (Fig. 5f), which can accommodate multiple HBV particles in their interior cavities (Fig. 5f and Supplementary Fig. 30).

To test the capacity of our shells to prevent a trapped virus from undergoing interactions with surfaces, we performed in vitro virus-blocking assays with HBV-binding antibodies immobilized on a solid surface (Fig. 5g and Supplementary Fig. 34). We quantified the extent of HBV core particle binding to the surface through the binding of orthogonal HBV core-specific reporter antibodies coupled to horseradish peroxidase (HRP). Residual HBV core particles that are bound to the surface are detected by HRP-catalysed production of a colourimetric signal. In the presence of our virus-engulfing shells (half $T=1$ shells), up to 99% of virus interactions with the surface were blocked (Fig. 5h), thus confirming the interaction-inhibiting capacity of our shells. Control experiments with shells lacking HBV-trapping antibodies resulted in minimal virus blocking compared with the signal generated by naked HBV core particles, which represents baseline 0% virus blocking.

HBV core particles directly incubated with antibodies, but without any shells present, were negligibly blocked from binding to the surface. This finding indicates that the antibodies by themselves do not fully passivate the HBV capsid surface even though they were added at 400-fold excess over the HBV particles. In contrast, when using shells functionalized with, on average, as few as five antibodies, we achieved a virus-blocking efficiency of greater than 80%. The blocking was nearly complete (up to 99%) when using more than five antibodies in the shells. The data thus show that the shell-trapping method can be highly effective even when only a handful of physical interactions are formed between the virus surface and surrounding shell. Our data indicate that the shells, and not the antibodies used for holding the virus inside the shell, shield the virus from its exterior by steric occlusion.

Virus neutralization in human cells

We investigated the neutralization capacity of the DNA origami half octahedron shells using adeno-associated virus serotype 2 (AAV2)[34] virions carrying an enhanced green fluorescent protein (eGFP) expression cassette[35] by both microscopy and flow cytometry (Fig. 6a). We stabilized DNA shells using UV point welding and PEG–oligolysine/oligolysine as described above. AAV2 particles were successfully trapped in DNA half shells functionalized with anti-AAV2 antibody in the shell interior, in serum in the presence of bovine serum albumin (BSA), as seen by direct imaging by negative stain TEM (Fig. 6b). The data also establish the modularity of the shell: by changing the virus-binding moieties one can trap different types of viruses.

We quantified the efficacy of virus neutralization by determining the dose-response curves for DNA half shells functionalized with on average 36 anti-AAV2 antibodies per half shell and free anti-AAV2 antibodies as reference (Supplementary Fig. 35). The number of eGFP positive cells, measured by flow cytometry analysis, served as a read-out for infection efficacy. The DNA half shells neutralized AAV2 with an estimated half maximal inhibitory concentration (IC_{50}) of ~0.3 nM (Supplementary Fig. 35). Under our conditions, the IC_{50} corresponded to approximately 2.5 half shells per infectious virus particle. The DNA half shells had increased neutralization capacity compared with the activity of the free anti-AAV2 (Fig. 6c,d and Supplementary Fig. 35). This enhanced neutralization is best appreciated in the fluorescence microscopy images (Fig. 6d), in which few eGFP positive cells remain in the samples with AAV2-trapping DNA half shells, whereas many eGFP positive cells appear in samples exposed to an identical dose of anti-AAV2 antibodies free in solution. This experiment demonstrates that the shells function in physiological conditions with live cells. It also shows that the shells can augment the already quite potent neutralization

capabilities of the anti-AAV2 antibodies. As discussed above for the in vitro HBV blocking experiments in Fig. 4, the enhanced neutralization suggests that the shells trap viruses in a multivalent fashion and that the shell material additionally contributes as a viral-surface occluding agent.

We also investigated whether the DNA origami half shells without any conjugated antibody had an effect, and we found a low but non-negligible neutralization activity at the highest origami concentration tested (Supplementary Fig. 35). We suggest this activity arises from electrostatic interactions between the PEG–oligolysine/oligolysine-coated DNA shells and the AAV2 particles. Finally, we explored whether exposure to the DNA half shells had any effect on cell viability and found no effect across any of the concentrations used in this study (Supplementary Fig. 35).

Outlook

We envision that trapping viruses in shells can decrease the viral load in acute viral infections by preventing viruses from interacting with host cells. We tested the virus-trapping concept successfully with HBV core and AAV2 virus particles. We achieved near complete inactivation by engulfing HBV core particles in a surrounding shell in vitro and could also effectively block AAV from infecting live cells. Owing to the modularity of the DNA shells, other virus binders could be used. For example, host receptor domains or peptides known to be targeted by a viral pathogen and DNA/RNA aptamers could be conjugated to the shells. One of our design solutions, the half $T=1$ shell, features 90 sites for anchoring virus-binding moieties in the interior cavity. This high level of multivalency will be particularly useful for trapping pathogens for which only low-affinity binders are available. Multiple different antibodies could also be combined to achieve higher specificity against a single target or against a plurality of targets.

Our icosahedral shells consist of DNA, which is durable, commercially available and easily functionalized and modified. The components needed for our shells can be mass-produced biotechnologically[36]. The use of DNA-based agents can potentially circumvent neutralization, phagocytosis and degradation by pathways of the innate and adaptive immune system targeting protein structures. We expect our shells to be largely non-toxic because they do not target any enzymes of the host metabolism as many current antivirals do. However, we cannot exclude that nucleic acid-specific reactions, such as the activation of pattern-recognition receptors recognizing DNA[37,38] or the induction of DNA-binding antibodies, may occur once the shells are applied in vivo. Testing our concept and assessing potentially adverse effects in organisms are important challenges for the future. Beyond the proposed application as virus traps, our programmable icosahedral canvas system also offers opportunities to create multivalent antigen carriers for vaccination, DNA or RNA carriers for gene therapy or gene modification, drug delivery vehicles and protective storage containers (for cargo loading examples, see Supplementary Fig. 36).

Online content

Any methods, additional references, Nature Research reporting summaries, source data, extended data, supplementary information, acknowledgements, peer review information; details of author contributions and competing interests; and statements of data and code availability are available at https://doi.org/10.1038/s41563-021-01020-4.

References

1. Lauster, D. et al. Phage capsid nanoparticles with defined ligand arrangement block influenza virus entry. *Nat. Nanotechnol.* **15**, 373–379 (2020).

2. Kwon, P. S. et al. Designer DNA architecture offers precise and multivalent spatial pattern-recognition for viral sensing and inhibition. *Nat. Chem.* **12**, 26–35 (2020).

3. Cao, L. et al. De novo design of picomolar SARS-CoV-2 miniprotein inhibitors. *Science* **370**, 426–431 (2020).

4. Cagno, V., Tseligka, E. D., Jones, S. T. & Tapparel, C. Heparan sulfate proteoglycans and viral attachment: true receptors or adaptation bias? *Viruses* **11**, 596 (2019).

5. Legendre, M. et al. Thirty-thousand-year-old distant relative of giant icosahedral DNA viruses with a pandoravirus morphology. *Proc. Natl Acad. Sci. USA* **111**, 4274–4279 (2014).

6. Bale, J. B. et al. Accurate design of megadalton-scale two-component icosahedral protein complexes. *Science* **353**, 389–394 (2016).

7. King, N. P. et al. Accurate design of co-assembling multi-component protein nanomaterials. *Nature* **510**, 103–108 (2014).

8. Lai, Y. T. et al. Structure of a designed protein cage that self-assembles into a highly porous cube. *Nat. Chem.* **6**, 1065–1071 (2014).

9. Butterfield, G. L. et al. Evolution of a designed protein assembly encapsulating its own RNA genome. *Nature* **552**, 415–420 (2017).

10. Rothemund, P. W. K. Folding DNA to create nanoscale shapes and patterns. *Nature* **440**, 297–302 (2006).

11. Douglas, S. M. et al. Self-assembly of DNA into nanoscale three-dimensional shapes. *Nature* **459**, 414–418 (2009).

12. Castro, C. E. et al. A primer to scaffolded DNA origami. *Nat. Methods* **8**, 221–229 (2011).

13. Veneziano, R. et al. Designer nanoscale DNA assemblies programmed from the top down. *Science* **352**, 1534 (2016).

14. Benson, E. et al. DNA rendering of polyhedral meshes at the nanoscale. *Nature* **523**, 441–444 (2015).

15. Dunn, K. E. et al. Guiding the folding pathway of DNA origami. *Nature* **525**, 82–86 (2015).

16. Bai, X. C., Martin, T. G., Scheres, S. H. & Dietz, H. Cryo-EM structure of a 3D DNA-origami object. *Proc. Natl Acad. Sci. USA* **109**, 20012–20017 (2012).

17. Funke, J. J. & Dietz, H. Placing molecules with Bohr radius resolution using DNA origami. *Nat. Nanotechnol.* **11**, 47–52 (2016).

18. Iinuma, R. et al. Polyhedra self-assembled from DNA tripods and characterized with 3D DNA-PAINT. *Science* **344**, 65–69 (2014).

19. Jungmann, R. et al. DNA origami-based nanoribbons: assembly, length distribution, and twist. *Nanotechnology* **22**, 275301 (2011).

20. Liu, W., Zhong, H., Wang, R. & Seeman, N. C. Crystalline two-dimensional DNA-origami arrays. *Angew. Chem. Int. Ed.* **50**, 264–267 (2011).

21. Suzuki, Y., Endo, M. & Sugiyama, H. Lipid-bilayer-assisted two-dimensional self-assembly of DNA origami nanostructures. *Nat. Commun.* **6**, 8052 (2015).

22. Ke, Y. et al. DNA brick crystals with prescribed depths. *Nat. Chem.* **6**, 994–1002 (2014).

23. Wagenbauer, K. F., Sigl, C. & Dietz, H. Gigadalton-scale shape-programmable DNA assemblies. *Nature* **552**, 78–83 (2017).

24. Crick, F. H. & Watson, J. D. Structure of small viruses. *Nature* **177**, 473–475 (1956).

25. Caspar, D. L. & Klug, A. Physical principles in the construction of regular viruses. *Cold Spring Harb. Symp. Quant. Biol.* **27**, 1–24 (1962).

26. Twarock, R. & Luque, A. Structural puzzles in virology solved with an overarching icosahedral design principle. *Nat. Commun.* **10**, 4414 (2019).

27. Gerling, T., Wagenbauer, K. F., Neuner, A. M. & Dietz, H. Dynamic DNA devices and assemblies formed by shape-complementary, non-base pairing 3D components. *Science* **347**, 1446–1452 (2015).

28. Douglas, S. M. et al. Rapid prototyping of 3D DNA-origami shapes with caDNAno. *Nucleic Acids Res.* **37**, 5001–5006 (2009).

29. Maffeo, C., Yoo, J. & Aksimentiev, A. De novo reconstruction of DNA origami structures through atomistic molecular dynamics simulation. *Nucleic Acids Res.* **44**, 3013–3019 (2016).

30. Wagenbauer, K. F. et al. How we make DNA origami. *ChemBioChem* **18**, 1873–1885 (2017).

31. Langecker, M. et al. Synthetic lipid membrane channels formed by designed DNA nanostructures. *Science* **338**, 932–936 (2012).

32. Gerling, T., Kube, M., Kick, B. & Dietz, H. Sequence-programmable covalent bonding of designed DNA assemblies. *Sci. Adv.* **4**, eaau1157 (2018).

33. Ponnuswamy, N. et al. Oligolysine-based coating protects DNA nanostructures from low-salt denaturation and nuclease degradation. *Nat. Commun.* **8**, 15654 (2017).

34. Wang, D., Tai, P. W. L. & Gao, G. Adeno-associated virus vector as a platform for gene therapy delivery. *Nat. Rev. Drug Discov.* **18**, 358–378 (2019).

35. Guo, P. et al. Rapid AAV-neutralizing antibody determination with a cell-binding assay. *Mol. Ther. Methods Clin. Dev.* **13**, 40–46 (2019).

36. Praetorius, F. et al. Biotechnological mass production of DNA origami. *Nature* **552**, 84–87 (2017).

37. Ohto, U. et al. Structural basis of CpG and inhibitory DNA recognition by Toll-like receptor 9. *Nature* **520**, 702–705 (2015).

38. Andreeva, L. et al. cGAS senses long and HMGB/TFAM-bound U-turn DNA by forming protein–DNA ladders. *Nature* **549**, 394–398 (2017).

Methods

Self-assembly of shell subunits. All self-assembly experiments were performed in standardized 'folding buffers' containing x mM $MgCl_2$ in addition to 5 mM Tris base, 1 mM EDTA and 5 mM NaCl at pH 8 (FoBx). Single-scaffold-chain DNA origami objects were self-assembled in one-pot folding reactions containing 50 nM scaffold DNA and 200 nM of each staple strand. The individual scaffolds were produced as described previously[39,40] (for sequences, see Supplementary Note). Folding buffer (FoB20) was used with $x = 20$ mM $MgCl_2$. All reaction mixtures were subjected to thermal annealing ramps in Tetrad (Bio-Rad) thermal cycling devices, as detailed in Supplementary Table 2. Staple strands were purchased from Integrated DNA Technologies.

Purification of shell subunits and self-assembly of shells. All shell subunits were purified by gel purification and, if necessary, concentrated by ultrafiltration (Amicon Ultra 500 μl with 100 kDa molecular weight cut-off) before self-assembling the subunits into shells. Both procedures were performed as previously described[30] with the following alterations. For gel purification, we used 1.5% agarose gels containing 0.5× TBE buffer (22.25 mM Tris base, 22.25 mM boric acid and 0.5 mM EDTA) and 5.5 mM $MgCl_2$. For ultrafiltration, the same filter was filled with the gel-purified sample multiple times (~2–5 times, ~400 μl each time) to increase the concentration of objects recovered from the filter. Before placing the filter upside down in a new filter tube, we performed two washing steps with 1× FoB5 (~400 μl) to achieve well-defined buffer conditions for the shell assembly. To assemble the purified (and concentrated) shell subunits into shells we adjusted the subunit and $MgCl_2$ concentrations by adding 1× FoB5 and 1.735 M $MgCl_2$ in suitable amounts. Typical subunit concentrations were in the range of 5–100 nM (for cryo-EM measurements, see Supplementary Table 3). Typical $MgCl_2$ concentrations for shell self-assembly were in the range of 10–40 mM. Shell self-assembly was performed at 40 °C. Reaction times were varied depending on the shell type (Fig. 3a). All the shell subunits and assembled shells can be stored at room temperature for several months.

$T = 1$ shell exterior modification. The $T = 1$ triangle and triangular brick (Fig. 2h) were dimerized using the ssDNA sticky ends protruding from the $T = 1$ triangle. The protruding sequences contained three thymidines for flexibility and seven-base-long sequence motifs that were directly complementary to the single-stranded scaffold domains of the brick (Supplementary Fig. 43b). Dimerization reactions were performed at room temperature overnight using a monomer concentration of 40 nM in the presence of 11 mM $MgCl_2$.

Cargo encapsulation in $T = 1$ shells. Nine staples of the $T = 1$ shell subunits were modified by adding 16 bases onto the 5′ ends. These nine modified staples and unmodified $T = 1$ staples were folded with the p8064 scaffold to produce $T = 1$ triangles with nine ssDNA 'handles' (Supplementary Fig. 36a, left). The 16-base ssDNA handles were located on the shell-inward facing surface of the monomers. Eight of those nine strands were oriented facing inwards towards the interior of the monomer and consequently may not have been accessible to the cargo. The ssDNA cargo was prepared by attaching staple strands to the p8064 ssDNA circular scaffold with a 16-base-long overhang that was complementary to the handles on the shell subunits. An oligonucleotide containing a CY5 dye was also hybridized to the scaffold to enable fluorescence read-out on laser scanning the agarose gels (Supplementary Fig. 36a, middle, and Supplementary Fig. 43c). To avoid having the unbound staples in the cargo solution, which would passivate the monomers, 20 different staples were mixed with the scaffolds in a 1:2 ratio. To anneal the staples to the circular ssDNA, FoB15 buffer was used with a temperature ramp of 65 °C for 15 min, followed by 60 to 44 °C at 1 °C h^{-1}. For proof-of-principle, we encapsulate gold nanoparticles by attaching complementary handles of the monomer's handles were attached to gold nanoparticles with a diameter of 30 nm (Cytodiagnostics, OligoREADY Gold Nanoparticle Conjugation Kit). A schematic and negative stain TEM tomogram slice are shown in Supplementary Fig. 36b,c. To increase the visibility of the encapsulated circular ssDNA in negative stain TEM images, gold nanoparticles with a diameter of 20 nm (Cytodiagnostics, OligoREADY Gold Nanoparticle Conjugation Kit) were attached to the circular ssDNA scaffold (schematic and negative stain TEM are shown in Supplementary Fig. 36b,c, last images from the right). $T = 1$ shells with and without cargo were assembled in 1× FoB20 buffer at 40 °C for 3 days. Shell subunits were gel-purified prior to assembly. The concentration of the triangles was 16 nM, and the concentration of the cargo (of any type) was 0.8 nM.

Half shells and HBV core binding. Nine staples on the inside of the triangles were modified with handles with 26 single-stranded bases at the 5′ ends (sequence: 5′-GCAGTAGAGTAGGTAGAGATTAGGCA-3′ oligonucleotide; for design details, see Supplementary Figs. 41 and 42). The triangles were purified and assembled as described above. Oligonucleotides complementary to the handle sequence and modified with a thiol group at the 3′ end were coupled to the antibody anti-HBc 17H7 (100 μg) using a sulfosuccinimidyl-4-(N-maleimidomethyl)cyclohexane-1-carboxylate crosslinker. The product was subsequently purified using proFIRE (Dynamic Biosensors). The DNA-modified antibodies were added to the assembled shells and incubated overnight at 25 °C.

HBV core particles were incubated with the modified shells for 1–4 h at 25 °C. To assemble $T = 1$ triangles around HBV core particles, the modified antibodies were added to single triangles. These triangles were then incubated with HBV core particles at a $MgCl_2$ concentration of 19 mM for 1 day.

Shell oligolysine stabilization. The complete octahedral shells were assembled with 35 mM $MgCl_2$ and UV-crosslinked as described previously[32] for 1 h using UV light with a wavelength of 310 nm from an Asahi Spectra Xenon Light source (300 W, MAX-303). The shells were incubated in a 0.6:1 ratio of N/P with a mixture of K_{10}-oligolysine and K_{10}-PEG$_{5K}$–oligolysine (1:1) for 1 h at room temperature as similarly described previously[33]. The octahedra were incubated in 55% mouse serum for 1 or 24 h at 37 °C. To allow imaging with negative stain, the samples were diluted with PBS to a final mouse serum concentration of 5% immediately before application to the negative stain grids.

The partial shells used for virus neutralization experiments in vivo were assembled with 60 mM $MgCl_2$ and UV-crosslinked as described previously[32] with UV light with a wavelength of 310 nm for 30 min using the Asahi Spectra Xenon Light source (300 W, MAX-303). We introduced three-base-long sticky overhangs at every stacking contact and added one thymidine at the ends of both oligonucleotides (Supplementary Fig. 45) to covalently crosslink the triangular subunits. The sticky overhangs were necessary to compensate for the decrease in blunt-end stacking induced by the addition of the thymidines for UV point welding. The shells were incubated in a 0.6:1 ratio of N/P with a mixture of K_{10}-oligolysine and K_{10}-PEG$_{5K}$–oligolysine (1:1) for 1 h at room temperature as similarly described previously[33]. The DNA-modified antibodies were added to the assembled shells and incubated overnight at room temperature.

Gel electrophoresis. The size distribution in the folding reactions or shell assemblies was investigated by agarose gel electrophoresis. For solutions including only shell subunits, we used 1.5% agarose gels containing 0.5× TBE buffer (22.25 mM Tris base, 22.25 mM boric acid, 0.5 mM EDTA) and 5.5 mM $MgCl_2$. For solutions including oligomeric assemblies such as shells, an agarose concentration of 0.5% was used. Gel electrophoresis was performed in 0.5× TBE buffers supplemented with the same $MgCl_2$ concentration as the solutions in which the shells were incubated. For $MgCl_2$ concentrations greater than 15 mM, a surrounding ice−water bath was used to cool the gel. Gel electrophoresis was performed for 1.5−2 h at a bias voltage of 90 V. For gels with $MgCl_2$ concentrations higher than 15 mM, we exchanged the buffer after 45 min. The agarose gels were then scanned with a Typhoon FLA 9500 laser scanner (GE Healthcare) with a pixel size of 50 μm per pixel.

Negative staining TEM. Samples were incubated on glow-discharged collodion-supported carbon-coated Cu400 TEM grids (in-house production) for 30−120 s depending on the structure and $MgCl_2$ concentration. The grids were stained with 2% aqueous uranyl formate solution containing 25 mM sodium hydroxide. Imaging was performed with magnifications between ×10,000 and ×42,000. $T = 3$ triangles were imaged with a Phillips CM100 transmission electron microscope equipped with an AMT 4Mpx CCD camera. All other negative staining data were acquired with SerialEM with a FEI Tecnai T12 microscope operated at 120 kV with a Tietz TEMCAM-F416 camera. TEM micrographs were high-pass filtered to remove long-range staining gradients, and the contrast was auto-levelled (Adobe Photoshop CS6). To obtain detailed information on individual particles and investigate successful encapsulation, negative stain EM tomography was used as a visualization technique. The grids were prepared as described above, and tilt series were acquired with magnifications between ×15,000 and ×30,000 using a FEI Tecnai 120 microscope. The stage was tilted from −50° to 50° and micrographs were acquired in 2° increments.

All tilt series were subsequently processed with Etomo (IMOD)[41] to acquire tomograms. The micrographs were aligned to each other by calculating a cross-correlation of the consecutive tilt series images. The tomogram was subsequently generated by filtered back-projection. The Gaussian filter used a cut-off of between 0.25 and 0.5 and a fall-off of 0.035.

Cryo-electron microscopy. The DNA origami concentrations used for preparing the cryo-EM grids are summarized in Supplementary Table 3. Samples with concentrations higher than 100 nM were applied to glow-discharged C-flat 1.2/1.3 or 2/1 thick grids (Protochip). Samples containing shells with less than 30 nM monomer concentration were incubated on glow-discharged grids with an ultrathin carbon film supported by a lacey carbon film on a 400-mesh copper grid (Ted Pella). The concentration of all single triangles increased to above 500 nM with PEG precipitation[30]. To prepare samples, 1 ml of the folding reaction (~50 nM monomer concentration) was mixed with 1 ml PEG, and the mixture was centrifuged at 21K relative centrifugal force (rcf) for 25 min and resuspended in 50−100 μl 1× FoB5. The DNA origami triangles used for assembling the shells were all gel-purified and concentrated by ultrafiltration, as described above, before increasing the $MgCl_2$ concentration. Plunge-freezing in liquid ethane was performed with a FEI Vitrobot Mark V instrument with a blot time of 1.5−2 s, a blot force of −1 and a drain time of 0 s at 22 °C and 100% humidity. The samples with less than 100 nM monomer concentration were incubated on

the support layer for 60–90 s before blotting. All cryo-EM images were acquired with a spherical-aberration (Cs)-corrected Titan Krios G2 electron microscope (Thermo Fisher) operated at 300 kV and equipped with a Falcon III 4k direct electron detector (Thermo Fisher). We used the software EPU 1.2 up to 2.6 (Thermo Fisher) for automated single particle acquisition. See Supplementary Table 3 for the microscope settings for all individual datasets. The defocus was set to −2 μm for all acquisitions. The image processing was first performed in RELION-2 (ref. [42]) and then later in RELION-3 (ref. [43]). The recorded movies were subjected to MotionCor2 (ref. [44]) for movie alignment and CTFFIND4.1 (ref. [45]) for contrast-transfer-function (CTF) estimation. After reference-free 2D classification, the best 2D class averages, as judged by visual inspection, were selected for further processing. A subset of these particles was used to calculate an initial model. After one to two rounds of 3D classification, the classes showing the most features or completely assembled shells were selected for 3D auto-refinement and post-processing. Octahedral (O) or icosahedral (I1) symmetry was used for the corresponding shells in the last two steps. All post-processed maps are deposited in the Electron Microscopy Data Bank (Supplementary Table 3).

In vitro virus-blocking ELISA assay. Various concentrations of assembled half $T = 1$ shells were incubated overnight at room temperature with 2 nM oligonucleotide-conjugated capture antibody (anti-HBc 17H7, isotype IgG-2b) in FoB30-T (FoB30 + 0.05% Tween-20). The next day the pre-incubated mixtures were added to 5 pM HBV core particles and incubated overnight at room temperature, yielding 1 nM capture antibody, 2.5 pM HBV core particles and 0–200 pM half $T = 1$ shells. A flat-bottomed, transparent, 96-well microplate (Nunc MaxiSorp) was treated overnight at 4 °C with 100 μl per well anti-IFA–HepBcore (1 μg ml⁻¹ in PBS). After washing four times with 200 μl per well PBS-T (PBS + 0.05% Tween-20), the well surface was blocked by incubating with 200 μl per well 5% BSA in PBS for 2 h at room temperature. After washing four times with 200 μl per well FoB30-T, 90 μl of the pre-incubated samples was added to each well and incubated for 2 h at room temperature, followed by washing and subsequent incubation for 1 h with 100 μl per well HRP-conjugated detection antibody (anti-HepBcore–HRP in FoB30-T). After washing with FoB30-T, 100 μl per well HRP substrate (3,3′,5,5′-tetramethylbenzidine, Life Technologies) was added and product formation was monitored over time by measuring the absorbance at 650 nm at intervals of 60 s using a plate reader pre-equilibrated to 30 °C (CLARIOstar, BMG LABTECH). HRP activity was calculated by fitting linear regression slopes to the linear region of the kinetic data (typically the first 5 min). Virus-blocking efficiency was calculated relative to a control of HBV core particles only and blank measurements in which no HBV core particles were present during all the incubation and washing steps. All experiments were performed in triplicate. The antibodies used for the ELISA assay were provided by the Centro De Ingenieria Genetica y Biotecnologia, Sancti Spiritus, in Cuba.

Helium ion microscopy. Imaging was performed with negative-stained TEM grids coated with a 5-nm layer of AuPd using a Quorum Q150T sputter coater in an ORION Nanofab microscope (Zeiss). We used an acceleration voltage of 30 kV and a beam current of 0.3–0.4 pA. The images were acquired in scanning mode with an Everhart–Thornley 2K detector.

Production of HBV core particles. HBV core particles of genotype D (subtype *ayw*2) were produced recombinantly in *Escherichia coli* K802 and BL21 cells (purchased from the Latvian Biomedical Research and Study Centre). Briefly, particles were obtained by sonication and clarification from bacterial protein extracts and purified by ammonium sulfate precipitation and subsequent anion-exchange and size-exclusion chromatography as described previously[46]. Final preparations were kept at a constant 4 °C in the dark in conventional PBS (including 0.05% NaN₃, 1 mM dithiothreitol).

Production of anti-HBc. Anti-HBV core antibody (anti-HBc) 17H7 (isotype IgG-2b) was produced by the Monoclonal Antibody Core Facility at the Helmholtz Zentrum München in Munich. Briefly, mouse HBc-recognizing B cells were generated by common hybridoma technology. The mice were challenged with the peptide NLEDPASRDLVV (aa 75–86 of the HBV core). Mouse hybridoma clones were selected and secreted antibodies were analysed by immune staining and precipitation of HBcAg, by the ELISA assay for native antigen recognition and by western blot analysis for the detection of denatured antigen. The final 17H7 preparations were purified by standard affinity chromatography using a protein A/G column and concentrated to 0.8 mg ml⁻¹ (5.33 μM) of protein and kept in conventional PBS (137 mM NaCl, 10 mM phosphate, 2.7 mM KCl, pH 7.4) at 4 °C in the dark.

Cell culture and neutralization assays. HEK293T cells (DSMZ) were cultured in Dulbecco's modified Eagle's medium (DMEM, Gibco, cat. no. 31966047) with 10% heat-inactivated fetal bovine serum (FBS, Sigma-Aldrich, cat. no. F9665). Cells were cultured routinely in a humidified incubator at 37 °C with 5% CO₂. AAV2 carrying eGFP (Biocat, cat. no. AA002-GVO-GC) was used for transduction experiments, in which the concentration of infectious particles was determined by titration as per the manufacturer's protocol. Briefly, cells were seeded in 24-well plates at 80,000 cells ml⁻¹ 16–24 h prior to transduction, and collected 72 h after transduction for quantification of the transduction efficiency by flow cytometry. Samples were acquired and analysed using an Attune NxT Flow Cytometer and software (Thermo Fisher), respectively. In total, 20,000 single cell events, gated on side scatter area versus height, were recorded for analysis. eGFP was excited with a 488-nm laser, and emission was measured with a 530/30-nm bandpass filter. Untreated cells were used as negative control. The concentration of infectious particles (or infectious units, IFU) was determined to be 1.23×10^9 IFU ml⁻¹. The total number of AAV2 virus particles (VP) was measured by ELISA as per the manufacturer's protocol (Progen, cat. no. PRATV), and determined to be 2.24×10^{12} VP ml⁻¹.

For the neutralization experiments, cells were cultured as above. Thus, 48-well plates were coated with poly-L-lysine (Sigma Aldrich, cat. no. P2636, 0.1 mg ml⁻¹, incubation for 10 min at room temperature) and then washed twice with H₂O and then PBS. HEK293T cells were seeded at 80,000 cells ml⁻¹ 16–24 h prior to transduction. Stock solutions were prepared for the overnight binding of conjugated anti-AAV2 to half-shell DNA origami. Binding occurred in the presence of 0.1 mg ml⁻¹ BSA. Conjugated anti-AAV2 and half shells without antibody were also prepared in an identical manner.

The next day, the half shells were coated with PEG–oligolysine/oligolysine by incubation at room temperature for 2 h. Next, each of the different titration conditions were prepared and diluted to a total of 33.5 μl per condition with PBS. Then, 4 μl of the diluted AAV2 sample (1:100, in PBS) was added and mixed, and the samples were left to incubate (2 h, room temperature). The cells were washed with PBS, and then 62.5 μl DMEM with 2% FBS was added to each well. The mixtures (37.5 μl) were then added dropwise to each well. The cells were incubated for 2 h before 100 μl DMEM with 18% FBS and 1× antibiotic/antimycotic was added. The cells were incubated for a further 22 h, the medium was removed, the cells were washed with 1× PBS and 250 μl DMEM with 10% FBS and 1× antibiotic/antimycotic was added. At 48 h post-transduction, the cells were trypsinized and prepared for flow cytometry analysis. The transduction efficiency was quantified by flow cytometry as described above; representative gates are given in Supplementary Fig. 46. Statistical analyses were performed with Graphpad Prism (GraphPad Software).

For epifluorescence imaging, the procedure was identical to above, with the exception that the cells were seeded in eight-chambered well slides (Nunc Lab-Tek, Thermo Fisher). After the total 48 h timepoint, the cells were washed with 1× PBS and then fixed with 2% paraformaldehyde. The cells were washed again (1× PBS), and the cell nuclei were stained (Hoescht 3342, diluted in PBS, 5 min, room temperature). The cells were washed with PBS, and the samples were mounted using Fluoromount-G aqueous mounting medium. The samples were imaged using a Tikon Eclipse Ti2-E inverted microscope with a ×10 objective. Images were collected using NIS-Elements AR software Version 5.02.01 (Nikon) and processed using ImageJ version 2.1.0.

Viability assay. Cytotoxicity was quantified by the cell viability following the incubation of cells with the half-shell mixtures for 24 or 48 h. HEK293T cells were seeded in poly-L-lysine-treated 96-well plates at 80,000 cells ml⁻¹. The cells were allowed to settle overnight, the medium was removed and the cells exposed to half-shell mixtures in an identical procedure to the neutralization assays. The cells were then incubated with half-shell solutions for a further 24 or 48 h, and alamarBlue reagent (Invitrogen, 10 μl per well) was added. The plates were mixed and incubated for 4 h before being read with a plate reader (CLARIOstar). Absorbance readings were taken at 570 and 600 nm, as per the manufacturer's protocol. The measured values were normalized to control wells, which were treated identically, but received PBS containing no origami structures. All conditions were measured at least in triplicate.

Statistics and reproducibility. All cryo-EM micrographs, negative stain TEM images and epifluorescent microscopy images presented in the manuscript and the Supplementary Information are exemplary micrographs and show representative images of many acquired micrographs. All negative stain TEM images, epifluorescent microscopy images and agarose gel electrophoresis experiments were repeated independently multiple times and reliably reproduced the same results.

Reporting Summary. Further information on research design is available in the Nature Research Reporting Summary linked to this article.

Data availability
Source data are provided with this paper. The remaining data supporting the findings of this study are available within the paper and its Supplementary Information files, and are available from the corresponding author upon reasonable request. The cryo-EM data from this study have been deposited in the Electron Microscopy Data Bank with the following accession codes: EMD-12007, EMD-12008, EMD-12009, EMD-12010, EMD-12011, EMD-12012, EMD-12013, EMD-12014, EMD-12015, EMD-12016, EMD-12019, EMD-12020, EMD-12021, EMD-12022, EMD-12023, EMD-12024, EMD-12044, EMD-12045, EMD-12046 and EMD-12049.

References

39. Engelhardt, F. A. S. et al. Custom-size, functional, and durable DNA origami with design-specific scaffolds. *ACS Nano* **13**, 5015–5027 (2019).
40. Kick, B., Praetorius, F., Dietz, H. & Weuster-Botz, D. Efficient production of single-stranded phage DNA as scaffolds for DNA origami. *Nano Lett.* **15**, 4672–4676 (2015).
41. Kremer, J. R., Mastronarde, D. N. & McIntosh, J. R. Computer visualization of three-dimensional image data using IMOD. *J. Struct. Biol.* **116**, 71–76 (1996).
42. Kimanius, D., Forsberg, B. O., Scheres, S. H. & Lindahl, E. Accelerated cryo-EM structure determination with parallelisation using GPUs in RELION-2. *Elife* **5**, e18722 (2016).
43. Zivanov, J. et al. New tools for automated high-resolution cryo-EM structure determination in RELION-3. *Elife* **7**, e42166 (2018).
44. Zheng, S. Q. et al. MotionCor2: anisotropic correction of beam-induced motion for improved cryo-electron microscopy. *Nat. Methods* **14**, 331–332 (2017).
45. Rohou, A. & Grigorieff, N. CTFFIND4: fast and accurate defocus estimation from electron micrographs. *J. Struct. Biol.* **192**, 216–221 (2015).
46. Sominskaya, I. et al. A VLP library of C-terminally truncated hepatitis B core proteins: correlation of RNA encapsidation with a Th1/Th2 switch in the immune responses of mice. *PLoS ONE* **8**, e75938 (2013).

Author contributions

H.D. designed the research. S.F. co-designed the icosahedral shell self-assembly studies (Figs. 1 and 2). C.S. performed shell subunit design, shell assembly and all structural studies (Figs. 1–6). E.M.W. performed shell modification and stabilization, and HBV virus-binding inhibition experiments (Figs. 4–6), supported by A.L. W.E. performed subunit exchange and HBV virus-binding inhibition experiments (Figs. 4 and 5). J.A.K. performed the cell culture AAV neutralization experiments (Fig. 6). K.S. performed auxiliary shell subunit geometry alteration experiments (Supplementary Fig. 18). F.K., F.W. and U.P. contributed HBV samples, and generated and provided anti-HBc (Fig. 5). S.A.A. performed cargo encapsulation (Supplementary Fig. 36). M.F.H. contributed to shell design choices.

Competing interests

A provisional patent has been filed by the TUM (PCT/EP2021/054307).

Additional information

Supplementary information The online version contains supplementary material available at https://doi.org/10.1038/s41563-021-01020-4.

Correspondence and requests for materials should be addressed to H.D.

Peer review information *Nature Materials* thanks Xing Wang, Andrew Ward, Hao Yan and Todd Yeates for their contribution to the peer review of this work.

Reprints and permissions information is available at www.nature.com/reprints.

Corresponding author(s): Hendrik Dietz

Last updated by author(s): Feb 15, 2021

Reporting Summary

Nature Research wishes to improve the reproducibility of the work that we publish. This form provides structure for consistency and transparency in reporting. For further information on Nature Research policies, see our Editorial Policies and the Editorial Policy Checklist.

Statistics

For all statistical analyses, confirm that the following items are present in the figure legend, table legend, main text, or Methods section.

n/a	Confirmed	
☐	☒	The exact sample size (*n*) for each experimental group/condition, given as a discrete number and unit of measurement
☐	☒	A statement on whether measurements were taken from distinct samples or whether the same sample was measured repeatedly
☐	☒	The statistical test(s) used AND whether they are one- or two-sided *Only common tests should be described solely by name; describe more complex techniques in the Methods section.*
☒	☐	A description of all covariates tested
☒	☐	A description of any assumptions or corrections, such as tests of normality and adjustment for multiple comparisons
☐	☒	A full description of the statistical parameters including central tendency (e.g. means) or other basic estimates (e.g. regression coefficient) AND variation (e.g. standard deviation) or associated estimates of uncertainty (e.g. confidence intervals)
☐	☒	For null hypothesis testing, the test statistic (e.g. *F*, *t*, *r*) with confidence intervals, effect sizes, degrees of freedom and *P* value noted *Give P values as exact values whenever suitable.*
☒	☐	For Bayesian analysis, information on the choice of priors and Markov chain Monte Carlo settings
☒	☐	For hierarchical and complex designs, identification of the appropriate level for tests and full reporting of outcomes
☒	☐	Estimates of effect sizes (e.g. Cohen's *d*, Pearson's *r*), indicating how they were calculated

Our web collection on statistics for biologists contains articles on many of the points above.

Software and code

Policy information about availability of computer code

Data collection	EPU 1.2 up to 2.6 (Thermo Fisher Scientific), SerialEM 3.5.6, Attune Nxt Software v3.1, NIS-Elements AR Ver5.02.01
Data analysis	RELION-2, RELION-3, CrYOLO v1, MotionCor 2, CTFFIND 4.1, UCSF Chimera 1.11.2, UCSF ChimeraX v0.1, Etomo 4.9.0 (Imod), Graphpad Prism v6.01, Attune Nxt Software v3.1, ImageJ v2.1.0/1.53c, caDNAno 2

For manuscripts utilizing custom algorithms or software that are central to the research but not yet described in published literature, software must be made available to editors and reviewers. We strongly encourage code deposition in a community repository (e.g. GitHub). See the Nature Research guidelines for submitting code & software for further information.

Data

Policy information about availability of data

All manuscripts must include a data availability statement. This statement should provide the following information, where applicable:
- Accession codes, unique identifiers, or web links for publicly available datasets
- A list of figures that have associated raw data
- A description of any restrictions on data availability

The data supporting the findings of this study are available within the paper and its supplementary information files and are available from the corresponding author upon reasonalbe request. Cryo-EM data of this study have been deposited in the Electron Microscopy Data Bank (EMDB) with accession codes: EMD-12007, EMD-12008, EMD-12009, EMD-12010, EMD-12011, EMD-12012, EMD-12013, EMD-12014, EMD-12015, EMD-12016, EMD-12019, EMD-12020, EMD-12021, EMD-12022, EMD-12023, EMD-12024, EMD-12044, EMD-12045, EMD-12046, EMD-12049

Field-specific reporting

Please select the one below that is the best fit for your research. If you are not sure, read the appropriate sections before making your selection.

☒ Life sciences ☐ Behavioural & social sciences ☐ Ecological, evolutionary & environmental sciences

For a reference copy of the document with all sections, see nature.com/documents/nr-reporting-summary-flat.pdf

Life sciences study design

All studies must disclose on these points even when the disclosure is negative.

Sample size	A sample size of 3 biological replicates was used to detect a significant difference (p<0.05) between groups with a signal to noise ratio of 3.0 with 80% power. For cryo-EM reconstructions, the sample size is dependent on the particle density per micrograph and the number of acquired micrographs which is limited by beam time. The number of particles was sufficient to reconstruct all acquired DNA-origami structures.
Data exclusions	No data was excluded. For cryo-EM reconstructions we manually sorted out damaged particles by 2D and 3D classification for the final refinement.
Replication	Experiments were performed multiple times to confirm the observations, the number of biological replicates is provided in the caption of the relevant figures. All attempts at replication were successful.
Randomization	Cells used for test experiments were randomly assigned to experimental groups in the process of sample preparation. For cryo-EM reconstructions all particles are randomly assigned to two groups which are reconstructed separately and merged after convergence in the final refinement.
Blinding	This is not relevant for the underlying study. Blinding was not used for cell experiments due to the use of automated collection and analysis systems, where the entire set of cytometry data was acquired and analyzed using identical parameters. Blinding was not performed for EM-micrographs and fluorescent microscopy experiments as they were not used for direct measurements or statistical analysis to justify blinding. The ELISA assay was essentially blinded as the samples were prepared and measured by different individuals.

Reporting for specific materials, systems and methods

We require information from authors about some types of materials, experimental systems and methods used in many studies. Here, indicate whether each material, system or method listed is relevant to your study. If you are not sure if a list item applies to your research, read the appropriate section before selecting a response.

Materials & experimental systems

n/a	Involved in the study
☐	☒ Antibodies
☐	☒ Eukaryotic cell lines
☒	☐ Palaeontology and archaeology
☒	☐ Animals and other organisms
☒	☐ Human research participants
☒	☐ Clinical data
☒	☐ Dual use research of concern

Methods

n/a	Involved in the study
☒	☐ ChIP-seq
☐	☒ Flow cytometry
☒	☐ MRI-based neuroimaging

Antibodies

Antibodies used	1) Anti-HBc , 17H7 Isotype IgG-2b, produced by MAB Monoclonal Antibody Core Facility of the Helmholtz Zentrum München - German Research Center for Environmental Health 2) Anti-IFA-HepBcore provided by Centro De Ingenieria Genetica y Biotecnologia de sancti spiritus in Cuba, Lot 161 3) Anti-HepBcore-HRP provided by Centro De Ingenieria Genetica y Biotecnologia de sancti spiritus in Cuba, Lot 171 4) Anti-AAV2 mouse recombinant, Progen Cat. No.: 610298, A20R, Lot: 810021-03
Validation	1) Anti-HBc (17H7 Isotype IgG-2b): Validated with immunostaining, precipitation reactions, ELISA experiments and Wesern Blot analysis (see Methods: Production of anti-HBc) 2) Anti-IFA-HepBcore: Validated with ELISA 3) Anti-HepBcore-HRP: Validated with ELISA 4) Anti-AAV2: "Validation: application confirmed" as provided by the supplier Progen (https://www.progen.com/anti-aav2-intact-particle-mouse-recombinant-a20r-lyophilized-purified.html)

Eukaryotic cell lines

Policy information about cell lines

Cell line source(s)	HEK293T cells were purchased from Leibniz Institute, DSMZ-German Collection of Microorganisms and Cull Cultures GmbH.
Authentication	Cell lines were kept at low passage and were not further authenticated.
Mycoplasma contamination	Cell lines tested negative for mycoplasma contamination.
Commonly misidentified lines (See ICLAC register)	No commonly misidentified cell lines were used.

Flow Cytometry

Plots

Confirm that:

☒ The axis labels state the marker and fluorochrome used (e.g. CD4-FITC).

☒ The axis scales are clearly visible. Include numbers along axes only for bottom left plot of group (a 'group' is an analysis of identical markers).

☒ All plots are contour plots with outliers or pseudocolor plots.

☒ A numerical value for number of cells or percentage (with statistics) is provided.

Methodology

Sample preparation	HEK293T cells were washed with PBS and trypsinized. Cells were then collected and fixed with 2% formaldehyde before being run on the flow cytometer.
Instrument	Attune NxT Flow Cytometer
Software	Attune NxT Flow Cytometer Software
Cell population abundance	20,000 single cells were analyzed for each condition.
Gating strategy	Cells were gated first by FSC/SSC, and then single cells were gated on SSC-A/SSC-H. Untreated cells were used as a negative control.

☒ Tick this box to confirm that a figure exemplifying the gating strategy is provided in the Supplementary Information.